# Concept Verification of Three-Layer DOI Detectors for Small Animal PET

Seong Jong Hong, Sun Il Kwon, Mikiko Ito, Geon Song Lee, Kwang-Souk Sim, Kwang Suk Park, June Tak Rhee, and Jae Sung Lee

***Abstract*—Improved spatial resolution without sacrificing sensitivity is one of the most challenging developmental goals for small animal PET scanners. The 3-layer configuration that we propose here utilizes relative offsets of half a crystal pitch in x- and y-directions, and pulse shape discrimination to obtain depth of interaction (DOI). Three layers of crystals with a dimension $1.5 \times 1.5 \times 7.0$ mm$^3$ were composed of a $L_{0.2}$ GSO ($Lu_{0.4}$ $Gd_{1.6}$ $SiO_4$: Ce) crystal layer and a $L_{0.9}$ GSO ($Lu_{1.8}$ $Gd_{0.2}$ $SiO_4$: Ce) crystal layer aligned with each other, and a $L_{0.9}$ GSO crystal layer offset at half a crystal pitch in x- and y-directions. The $L_{0.9}$ GSO crystal layer was attached to a Hamamatsu H9500 flat-panel PMT. The devised small animal PET scanner has a diameter of 84 mm with one detector ring, and can be upgraded to two detector rings. GEANT4 Monte-Carlo simulation was used to estimate sensitivities of $\sim 12\%$ and $\sim 20\%$, respectively, at the center of one and two PMT ring system with an energy window of 350 $\sim$ 750 keV. We present flood images with peak-to-valley ratios of about 5–6 obtained using $^{22}$ Na and layer identification capability of $\sim 99\%$ with pulse shape analysis, and verified the basic concepts of multi-layer small animal PET.**

***Index Terms*—Animal PET, depth of interaction (DOI), lutetium gadolinium oxyorthosilicate (LGSO), three-layer crystal.**

## I. Introduction

MOST molecular imaging research is undertaken using small animals, which provide a conduit between *in vitro* or *ex vivo* studies and human clinical imaging. Therefore, there are increasing demands for small animal imaging devices with enhanced performance characteristics, e.g., resolution and sensitivity, which are substantially better than those of commercial human scanners [1], [2]. Since a typical human weighs about 70-kg and a mouse 30-g, a mouse organ can be visualized with the same clarity if the spatial resolution of the small animal scanner used is about 10 times better than that of a human scanner [3], [4]. To achieve higher spatial resolutions, each image-pixel produced by a small animal scanner should contain the same number of events as that of a human scanner. Although higher radiation doses can achieve the same number of events in image-pixels in theory, such higher radiation doses are undesirable especially for longitudinal studies in small animals since such higher radiation levels are likely to be unbearable to the small animals. Considering that the typical sensitivity of a human scanner is about 0.3%, small animal scanners would have poorer image qualities than human scanners even at a sensitivity of 30%. Therefore it is very important to increase the sensitivity of small animal scanners. The goal of our work was to design a small animal PET scanner with a spatial resolution of 1–2 mm and an order of sensitivity of 10%, and to verify the basic concepts of small animal PET scanning.

During recent years, several small animal PET scanners have been developed for molecular imaging research. A small animal PET scanner (microPET) was developed by the UCLA group [4], and subsequent systems have used a single layer of crystals of length 10 mm [5], [6]. Even though the microPET achieved an 1–2 mm radial resolution at the center of the system, this resolution rapidly deteriorated to $\sim$ 3 mm at large radii due to parallax error. This compelled to use short crystals, which resulted in a sensitivity reduction [4], [6]. Therefore, improving spatial resolution without sacrificing sensitivity has been one of the most challenging goals for small animal PET scanners. The most recent scanners, such as, the ClearPET and GE Explorer Vista PET use two layers of crystals to reduce parallax errors at large radii [7], [8]. One of the approaches used to achieve this goal was to use crystals with different timing properties, such as, LSO and LuYAP [9]. Using this approach, LSO crystals are aligned to match LuYAP crystals. Another approach involves the offsetting of the first layer of crystals relative to the second layer, and to use the same type of crystals for both layers [10], [11].

We undertook to combine these two approaches and to construct a 3-layer small animal PET scanner, so as to improve spatial resolution and DOI without sacrificing sensitivity [12], [13]. In this paper, we present the recent progress made toward the development of the 3-layer PET scanner using LGSO crystals (Hitachi Chemical Co., Ltd., Ibaraki, Japan) [14] and Hamamatsu H9500 PMTs. It should be noted that this concept can be extended to a 4-layer small animal PET scanner. We

Manuscript received August 17, 2007; revised November 15, 2007. This work was supported by Grants from the Basic Research Program (R01-2006-000-10296-0) and the Atomic Energy R&D Program (M20704000015-07M0400-01512) of the Korean Science and Engineering Foundation (KOSEF).

S. J. Hong is with the Institute of Radiation Medicine, Medical Research Center, Seoul National University College of Medicine, Seoul 110-744, Korea.

S. I. Kwon is with the Department of Nuclear Medicine and Interdisciplinary Programs in Radiation Applied Life Science Major, Seoul National University College of Medicine, Seoul 110-744, Korea.

M. Ito and K.-S. Sim are with the Department of Physics, Korea University, Seoul 136-701, Korea.

G. S. Lee and K. S. Park are with the Department of Biomedical Engineering, Seoul National University College of Medicine, Seoul 110-744, Korea.

J. T. Rhee is with the Department of Physics, Konkuk University, Seoul 143-701, Korea.

J. S. Lee is with the Institute of Radiation Medicine, Medical Research Center, and the Departments of Nuclear Medicine and Biomedical Sciences and Interdisciplinary Programs in Radiation Applied Life Science Major, Seoul National University College of Medicine, Seoul 110-744, Korea (e-mail: jaes@snu.ac.kr).

Color versions of one or more of the figures in this paper are available online at http://ieeexplore.ieee.org.

Digital Object Identifier 10.1109/TNS.2008.920258

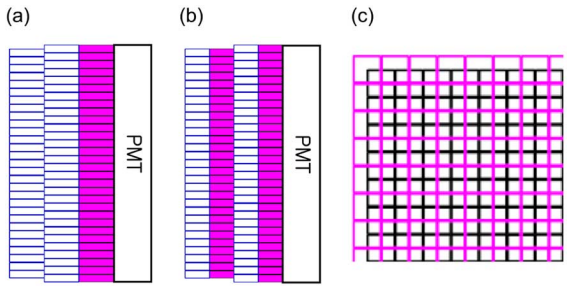


Fig. 1. Animal PET configuration with 3- or 4-layer of crystals, and an overhead view of the part of the 3- or 4-layer configurations. (a) 3-layer configuration. (b) 4-layer configuration. (c) Overhead view of the part of the 3- or 4-layer PET scanner.

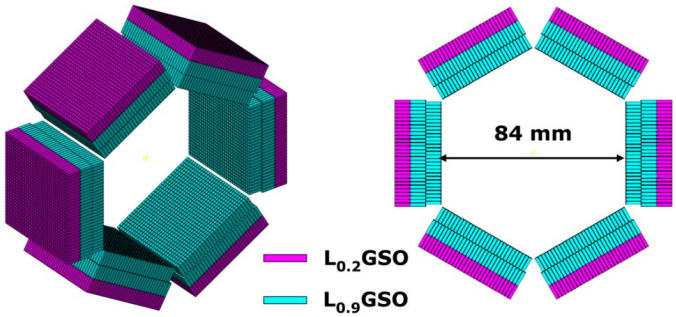


Fig. 2. Animal PET configuration with three layers of crystals. The height of each crystal is 7 mm.

would like to note that a similar 4-layer small animal PET scanner using a light sharing scheme has been proposed to achieve a high sensitivity with DOI capability [15], [16].

## II. Materials and Methods

### A. Detector Configuration

Our proposal of combining these two approaches, one that employs different crystal timing properties [9] and the other that uses offset crystals [10], [11], is shown schematically in Fig. 1(a) for a 3-layer configuration, and in Fig. 1(b) for a 4-layer configuration. Fig. 1(c) shows an overhead view of the part of the 3- and 4-layer configurations in which the offset is made in x- and y-directions.

The 3-layer configuration that we propose is shown in Fig. 2. This employs aligned 7-mm long $L_{0.2}$ GSO and 7-mm long $L_{0.9}$ GSO crystal layers, and a 7-mm long $L_{0.9}$ GSO crystal layer with the offset of half a crystal pitch in x- and y-directions relative to the aligned two crystal layers. The $L_{0.2}$ GSO crystal layer is attached to the H9500 PMT (Hamamatsu Photonics K.K., Japan) which has a dimension of $52 \times 52$ mm$^2$ and an effective area of $49 \times 49$ mm$^2$. The cross section area of $1.5 \times 1.5$ mm$^2$ for all crystals was chosen to obtain a 1–2 mm spatial resolution at the center of the scanner. The gap between crystals was filled with a layer of 3M Enhanced Spectral Reflector (ESR) polymer of thickness 0.065 mm, resulting in the crystal pitch of $\sim 1.57$ mm and the packing fraction of 0.91. The proposed 3-layer small animal PET system consists of the inner most $L_{0.9}$ GSO crystal layer with $29 \times 29$ crystals, and the other two $L_{0.2}$ GSO and $L_{0.9}$ GSO crystal layers each with $30 \times 30$ crystals.

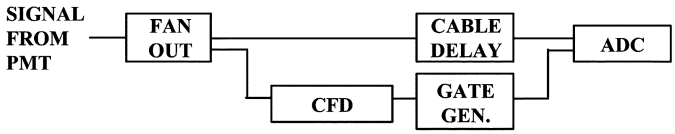


Fig. 3. Schematic diagram of data flow.

### B. Monte-Carlo Simulation

We used the GEANT4 Monte-Carlo program to estimate sensitivity. A simulated $^{18}$F source of cylindrical shape (diameter 0.1 mm and length 0.1 mm) was placed at 0.0, 10.0, 20.0, 30.0, 40.0 and 50.0 mm in the radial and axial directions from the center of the small animal PET scanner. The source was surrounded by cylindrical tissue of diameter 2.0 mm and length 2.0 mm. The positrons emitted by $^{18}$F were assumed to have a kinetic energy of 250 keV (the average energy of emitted positrons). We simulated two cases; one detector ring with 6 PMTs (Fig. 2), and two detector rings with 12 PMTs.

### C. Crystal Testing

Crystals that generate a large amount of scintillation photons with different timing properties would be optimal for a 3-layer animal PET configuration. However, since the 3-layer animal PET scanner would have sensitivity of the order of 10%, the decay time of the crystals should not be excessive.

We tested several different crystals, i.e., LuYAP ($Lu_{0.7}$ $Y_{0.3}$ $AlO_3$: Ce), LYSO ($Lu_{1.8}$ $Y_{0.2}$ $SiO_5$ :Ce), $L_{0.2}$ GSO, and $L_{0.9}$ GSO, with a Hamamatsu H2451-50 PMT using a VME/NIM data acquisition system. The sizes of crystals were $2.0 \times 2.0 \times 7.0$ mm$^3$ for LuYAP and LYSO crystals, and $1.5 \times 1.5 \times 7.0$ mm$^3$ for $L_{0.2}$ GSO, and $L_{0.9}$ GSO crystals. All the faces of the crystals were polished. Fig. 3 shows a data flow diagram of the test setup used to measure energy resolutions. A signal from the PMT was used to generate the ADC GATE signal of 300 ns. To discriminate signals and noise, we used a CAEN N485 NIM module for constant fraction discrimination. In addition, we used a CAEN V965 VME ADC module, which measures integrated charge up to 800 pC with a 200 fC/bit resolution. The crystals were wrapped with three layers of 3M ESR polymer, except for the surface facing the PMT.

### D. Crystal Wrapping with 3M ESR Polymer

The 3-layer animal PET scanner in Fig. 2 requires about 15 000 crystals with a miniature size of $1.5 \times 1.5 \times 7.0$ mm$^3$. Because it would have been time-consuming and impractical to have wrapped these crystals individually, we chose the grid method proposed by the Washington group [17], which involves the preparation of 3M ESR strips, as shown in Fig. 4(a) or 4(b), and the assembly of a grid, as shown in Fig. 4(c). Since each crystal was inserted into a square of the assembled grid, the gap between crystals were essentially filled with one layer of 3M ESR polymer.

It is important that crystals be precisely arranged in each crystal layer and between crystal layers in the 3-layer animal PET scanner, because misalignment of the crystals would cause difficulties identifying crystals struck by annihilation photons.

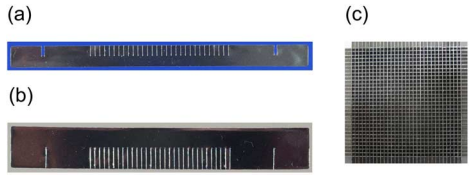


Fig. 4. Prepared ESR strips made from 3M ESR, and the constructed aluminum grid. (a) ESR strip for 7-mm crystals. (b) ESR strip for 14-mm crystals. (c) Grid made of aluminum.

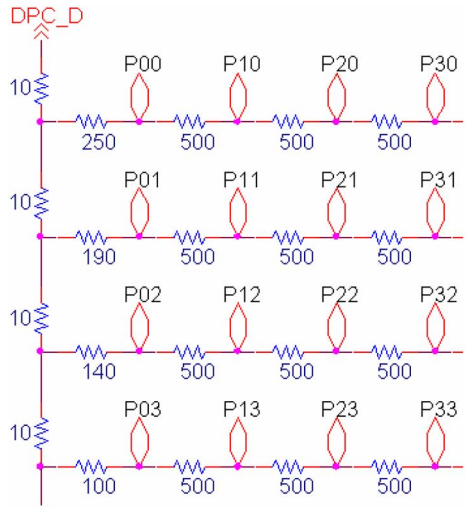


Fig. 5. Part of the charge division circuit diagram.

The grid method is an easier method of obtaining precise alignment than individual wrapping, because as crystal sizes become smaller, precise alignments of crystal layers become more difficult. To reduce the number of crystal layer alignments, we produced a 14-mm long strip shown in Fig. 4(b), so that two crystals could be inserted into the same square of the grid, thus guaranteeing the alignments of $L_{0.2}$ GSO and $L_{0.9}$ GSO crystals.

### *E. Charge Division Circuit and Flood Image*

The H9500 PMT produces 256 anode signals, which are difficult to handle. Thus, to reduce this number to 4 signals and still obtain information on positions struck by photons, we built a charge division circuit consisted of a resistor matrix [18]. Fig. 5 shows the part of the charge division circuit diagram, which also shows one of the 4 signals. The charge division circuit produces 6 outputs; the 4 outputs to obtain positions struck by photons, one output for the analog sum of the 4 outputs, and finally one output for the dynode signal of the H9500 PMT. The dynode signal was used to generate trigger signals, which in turn generated the ADC GATE and the TDC START signals.

To verify the concept of the proposed animal PET, we assembled a $7 \times 7$ $L_{0.9}$ GSO crystal block and a $6 \times 6$ $L_{0.9}$ GSO crystal block using the grid method and irradiated the crystal blocks with a $3.7 \times 10^5$ $Bq^{22}$ Na radiation source. The $6 \times 6$ $L_{0.9}$ GSO crystal block was positioned above the $7 \times 7$ $L_{0.9}$ GSO crystal block with an offset of half a crystal pitch in x- and y-directions. The 2-layer crystal block was mounted on the

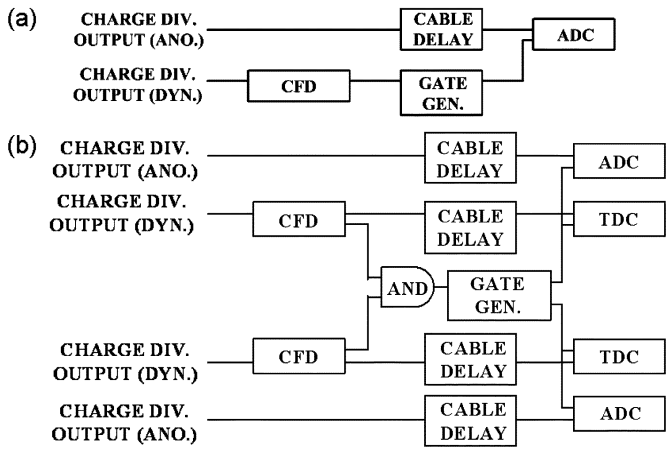


Fig. 6. Schematic diagram of data flow. (a) For flood image. (b) To measure ADC and TDC.

H9500 PMT, facing the $7 \times 7$ $L_{0.9}$ GSO crystal block of the PMT. Optical grease was applied between the 2-layer crystal block and the H9500 PMT, and between the $7 \times 7$ and the $6 \times 6$ $L_{0.9}$ GSO crystal blocks. We also built a second $7 \times 7$ $L_{0.9}$ GSO crystal block using the same method to make coincidence measurements possible.

Fig. 6 shows the data flow diagram of the test setup used to measure energy and coincidence time resolutions. Dynode signals were used to generate coincidence signals, ADC GATE, and TDC START signals. Appropriate lengths of cables were added to ensure that signals arrived within the ADC GATE of 300 ns and that the TDC START pulses arrived before the TDC STOP pulses. To discriminate signals from noise, we used a CAEN N485 NIM module for constant fraction discrimination. In addition, we used a CAEN V965 VME ADC module to measure integrated charges and a CAEN V775N VME TDC module to measure arrival time differences between START and STOP pulses. Positions struck by photons were determined with the Anger-type calculation using the 4 signals from the charge division circuit to obtain a flood image [18].

### *F. Layer Identification Using Pulse Shape Analysis*

Fig. 7, provided by Hitachi Chemicals, shows the timing properties of the $L_{0.2}$ GSO and $L_{0.9}$ GSO crystals. The difference between the decay times of these crystals is sufficient to enable crystals struck by gamma rays to be identified by using the pulse shape discrimination. The decay times of these crystals are also rapid enough to realize the 3-layer animal PET scanner with high sensitivity.

The 2-layer crystal block used to measure the flood image was again used for the layer identification using pulse shape analysis. After shaping the dynode signals from H9500 using Nyquist filters, we used a CAEN V729 40-MHz sampling ADC to sample the filtered pulses every 25 ns. The depth of interaction between the aligned $L_{0.2}$ GSO and $L_{0.9}$ GSO crystal layers was identified using the ratio of the largest sampled value (maximum height) over the total value up to 400 ns.

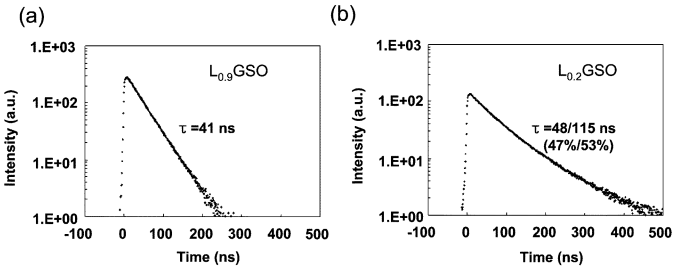


Fig. 7. Pulse characteristics of $L_{0.9}$ GSO and $L_{0.2}$ GSO crystals (courtesy of Dr. Ishibashi at Hitachi Chemical Co., Ltd.)

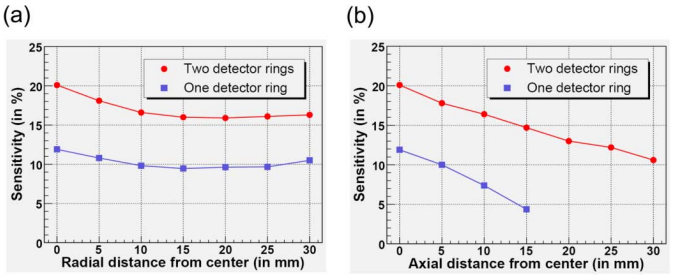


Fig. 8. Expected sensitivities: (a) Radial sensitivities. (b) Axial sensitivities. The lower and upper lines show the sensitivities of one and two detector rings, respectively.

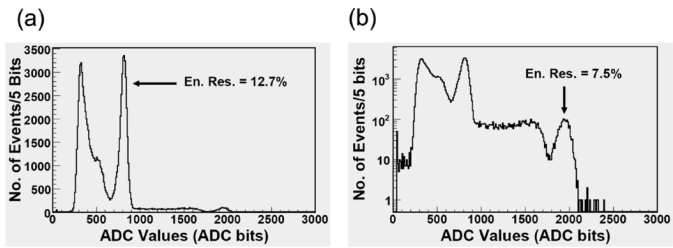


Fig. 9. ADC distributions obtained for H2453 PMT-$L_{0.9}$ GSO crystals. The arrow indicates the peak to obtain the energy resolution. (a) Linear y-scale. (b) Log y-scale.

## III. Results

### A. Sensitivity by Monte Carlo Simulation

Fig. 8 represents the expected sensitivity of the animal PET system as a function of radial and axial distance, and shows an $\sim$ 12% sensitivity for one detector ring and a sensitivity of $\sim$ 20% for two detector rings at the center of the system. We required both of total energy deposits to be between 350 and 750 keV. The total energy deposit was obtained by summing individual energy deposits in the same crystal layer of a PMT.

### B. Crystal Tests

Fig. 9(a) shows an ADC distribution obtained using the H2453 PMT-$L_{0.9}$ GSO coupling. The energy resolution of 12.7 % was determined by fitting the photoelectric peak at 511 keV, and assuming a Gaussian distribution. Fig. 10(b), which has a log-y scale, and also shows the photoelectric peak of 1.275-MeV photons emitted from $^{22}$ Na, with an energy resolution of 7.5%.

Fig. 10(a) and Fig. 10(b) show ADC distributions obtained from the H2453 PMT-$L_{0.2}$ GSO and the H2453 PMT-LuYAP

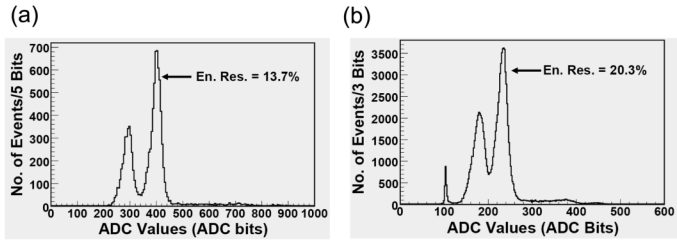


Fig. 10. ADC distributions obtained for H2453 PMT-$L_{0.2}$ GSO and LuYAP crystals. The arrow indicates the peak to obtain the energy resolution. (a) $L_{0.2}$ GSO. (b) LuYAP.

TABLE I
Energy Resolutions and Peak Values

| Scintillation Crystal | Energy Resolution (FWHM, %) | 511-keV Peak Value (ADC bits) |
|---|---|---|
| $L_{0.9}$GSO | 12.7 | 708 |
| $L_{0.2}$GSO | 13.7 | 300 |
| LYSO | 16.4 | 626 |
| LuYAP | 20.3 | 132 |

couplings, respectively. We obtained energy resolutions of 13.7% for $L_{0.2}$ GSO, 20.3% for LuYAP, and 16.4% for LYSO. Since the energy resolution for LYSO was slightly worse than reported [16], [19], we tested several other crystals from the same delivery, but obtained similar resolutions.

The light yields of crystals are also important, as the same threshold level required to reject noises and scatter events has to be applied for each PMT. Table I presents summaries of energy resolutions and peak values at 511 keV for various crystals, which were obtained with taking into account of ADC offset values. Based on these results, $L_{0.9}$ GSO and $L_{0.2}$ GSO were chosen to be the primary candidate crystals of the 3-layer animal PET system.

### C. Flood Image

Fig. 11(a) presents the flood image of the 2-layer $7 \times 7$ $L_{0.9}$ GSO crystal block and of the $6 \times 6$ $L_{0.9}$ GSO crystal block, measured at the center of the H9500 PMT, and shows the clear separation of individual crystals. Horizontal and vertical projection diagrams are also given in Fig. 11(b) and (c), which also show that peak-to-valley ratios were about $7 \sim 8$. Fig. 12 presents a flood image, and its projection histograms obtained at the corner of the H9500 PMT, and also shows a clear separation of individual crystals. The peak-to-valley ratios were about 5–6, except for the edge of the H9500 PMT, lower than at the center. The top-left crystal cell represented by the box in Fig. 12 appeared in a wrong position, which turned out to be caused by a damaged polymer between two crystals. The correct position was indicated by the black dot in Fig. 12.

Energy resolutions from the events in the boxes indicated in Fig. 11 were 14.4% for the $6 \times 6$ $L_{0.9}$ GSO crystals and 18.1% for the $7 \times 7$ $L_{0.9}$ GSO crystals. The peak values at 511 keV for the $6 \times 6$ $L_{0.9}$ GSO crystals were lower by 9% than those for the $7 \times 7$ $L_{0.9}$ GSO crystals, which was caused by the scintillation light loss at the gaps between the $7 \times 7$ $L_{0.9}$ GSO crystals. The worse energy resolution for the $7 \times 7$ $L_{0.9}$ GSO crystals than for

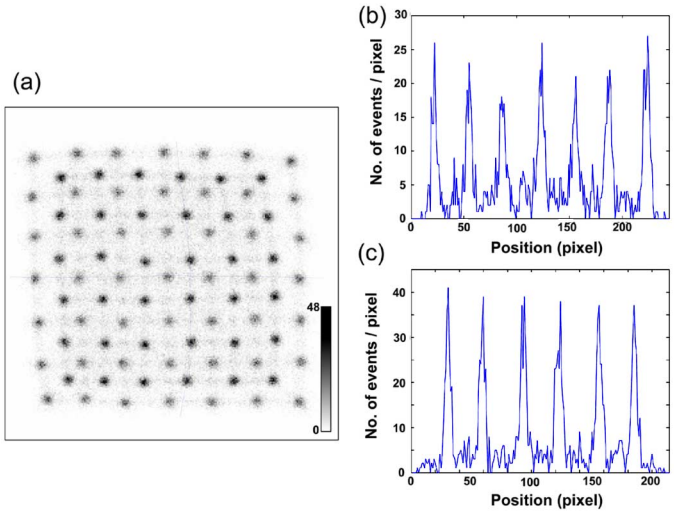


Fig. 11. Flood image at the corner of the H9500 PMT, and its horizontal and vertical projection histograms. The gray scale bar represents a number of events in each cell of the flood image which consists of 256 × 256 cells. The flood image was obtained (a) Flood image. (b) Horizontal projection histogram. (c) Vertical projection histogram.

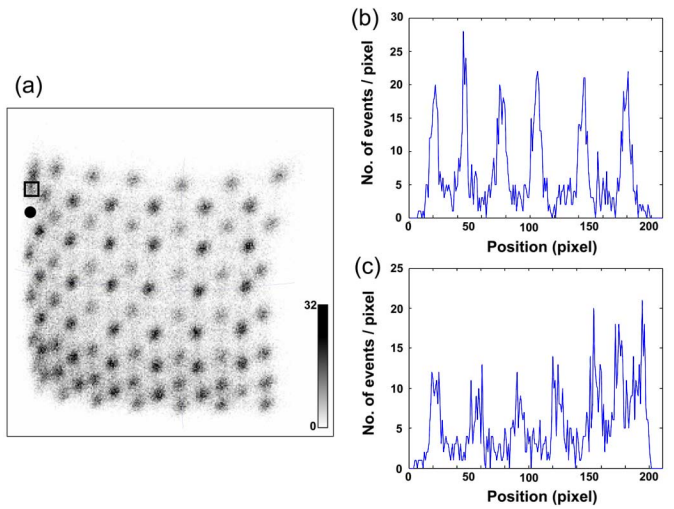


Fig. 12. Flood image at the corner of the H9500 PMT, and its horizontal and vertical projection histograms. The gray scale bar represents a number of events in each cell of the flood image which consists of 256 × 256 cells. (a) Flood image. (b) Horizontal projection histogram. (c) Vertical projection histogram.

the 6 × 6 $L_{0.9}$ GSO crystals might have been caused by scattered events. We obtained a coincidence time resolution of 1.0 ns from two H9500 PMTs; one with the 2-layer crystal block and the other with a single layer 7 × 7 $L_{0.9}$ GSO crystal block.

### *D. Layer Identification Using Pulse Shape Analysis*

Fig. 13 shows the normalized pulse shapes for $L_{0.9}$ GSO and $L_{0.2}$ GSO crystals obtained with the CAEN V729 40-MHz sampling ADC, respectively. The Nyquist filters preserved fast components of rising edges and produced long pulses which may not be optimal for high rates. Fig. 14(a) and Fig. 14(b) show the scatter plot and the ratio of the largest sampled value and the total value of first 16 samples, respectively. An energy cut of 10 000 ADC bits was selected to include the photoelectric peak from $L_{0.2}$ GSO crystals, which have lower light yields than $L_{0.9}$

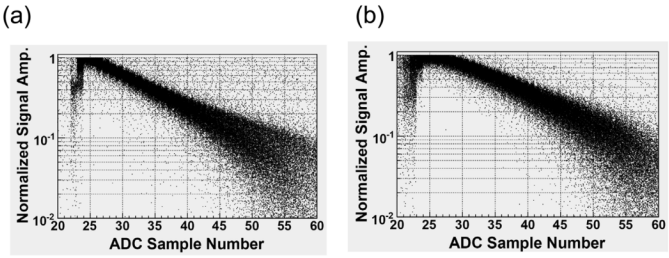


Fig. 13. Normalized pulse shapes for $L_{0.9}$ GSO and $L_{0.2}$ GSO crystals, sampled with a 25-ns interval.

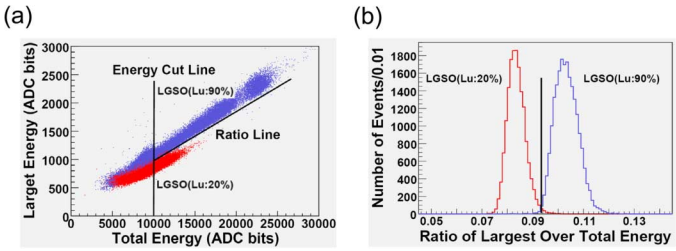


Fig. 14. Crystal identification. (a) Total energy versus the largest energy of the sampled values. (b) Ratios of the largest over the total energy.

GSO crystals. We achieved crystal identification efficiencies of ∼ 99%. The method proposed by the ClearPET group which compares the 16th sample over the summed sampled value resulted in poor identification efficiencies of 85% for $L_{0.2}$ GSO and 72% for $L_{0.9}$ GSO, compared to above 98% efficiencies for LuYAP and LYSO by the ClearPET group [9]. The discrepancy could have been caused by different Nyquist filters and crystals.

## IV. Summary and Conclusion

The Monte-Carlo simulation showed the ∼ 12% sensitivity for one detector ring and the ∼ 20% sensitivity for two detector rings at the center of the small animal PET system, respectively. The flood image obtained using the charge-division circuit and H9500 showed a clear separation of crystals in the central area of the H9500 PMT, with the peak-to-valley ratios of 5 ∼ 6. The identification efficiencies of the $L_{0.2}$ GSO and $L_{0.9}$ GSO crystal layers were ∼ 99%.

In reality, achieving these high sensitivities requires as little dead time as possible in data acquisition. Even though we have shown very good DOI capability with three layers of 1.5 × 1.5 × 7.0 $mm^3$ crystals, realizing good spatial resolution and sensitivity may be challenging due to many scattered events in this fine crystal. In this report, energy and time resolutions were measured using the CAEN V965 ADC and the CAEN V775 TDC, respectively, which we plan to replace with custom-designed electronics boards. The length of the shaped pulses was also almost 1 $\mu$s which may not be ideal for the high efficiency 3-layer animal PET system. We are currently working on to employ different Nyquist filters to shorten the shaped pulses and to measure energy resolutions using the shaped pulses with a 100-MHz sampling ADC. Even though more works need to be done, we are confident that a 3-layer animal PET scanner with high resolution and sensitivity can be built.

## ACKNOWLEDGMENT

The authors would like to thank J. H. Choi from Konkuk University for assembling crystal layers for this study.

## REFERENCES

[1] Y. C. Tai and R. Laforest, "Instrumentation aspects of animal PET," *Annu. Rev. Biomed. Eng.*, vol. 7, pp. 255–285, 2005.

[2] M. G. Pomper and J. S. Lee JS, "Small animal imaging in drug development," *Curr. Pharm. Des.*, vol. 11, pp. 3247–3272, 2005.

[3] M. V. Green, J. Seidel, J. J. Vaquero, E. Jagoda, I. Lee, and W. C. Eckelman, "High resolution PET, SPECT and projection imaging in small animals," *Comput. Med. Imaging Graph.*, vol. 25, pp. 79–86, 2001.

[4] J. S. Kim, J. S. Lee, K. C. Im, S. J. Kim, S.-Y. Kim, D. S. Lee, and D. H. Moon, "Performance measurement of the microPET Focus 120," in *J. Nucl. Med.*, to be published.

[5] S. R. Cherry, Y. Shao, R. W. Silverman, K. Meadors, S. Siegel, A. Chatziioannou, J. W. Young, W. Jones, J. C. Moyers, D. Newport, A. Boutefnouchet, T. H. Farquhar, M. Andreaco, M. J. Paulus, D. M. Binkley, R. Nutt, and M. E. Phelps, "MicroPET: A high resolution PET scanner for imaging small animals," *IEEE Trans. Nucl. Sci.*, vol. 44, no. 3, pp. 1161–1166, Jun. 1997.

[6] C. Knoess, S. Siegel, A. Smith, D. Newport, N. Richerzhagen, A. Winkeler, A. Jacobs, R. N. Goble, R. Graf, K. Wienhard, and W. D. Heiss, "Performance evaluation of the microPET R4 PET scanner for rodents," *Eur. J. Nucl. Med. Mol. Imaging*, vol. 30, no. 5, pp. 737–747, 2003.

[7] U. Heinrichs, U. Pietrzyk, and K. Ziemons, "Design optimization of the PMT-ClearPET prototypes based on simulation studies with GEANT3," *IEEE Trans. Nucl. Sci.*, vol. 50, no. 5, pp. 1428–1432, Oct. 2003.

[8] Y. Wang, J. Seidel, B. M. Tsui, J. J. Vaquero, and M. G. Pomper, "Performance evaluation of the GE healthcare eXplore VISTA dual-ring small-animal PET scanner," *J. Nucl. Med.*, vol. 47, pp. 1891–1900, 2006.

[9] M. Streun, G. Brandenburg, H. Larue, H. Saleh, E. Zimmermann, K. Ziemons, and H. Halling, "Pulse shape discrimination of LSO and LuYAP scintillators for depth of interaction detection in PET," *IEEE Trans. Nucl. Sci.*, vol. 50, no. 3, pp. 344–347, Jun. 2003.

[10] H. Liu, T. Omura, M. Watanabe, and T. Yamashita, "Development of a depth of interaction detector for $\gamma$ -rays," *Nucl. Instrum. Methods*, vol. A 459, pp. 182–190, 2001.

[11] N. Zhang, C. J. Thompson, F. Cayouette, D. Jolly, and S. Kecani, "A prorotype modular detector design for high resolution positron emission mammography imaging," *IEEE Trans. Nucl. Sci.*, vol. 50, no. 5, pp. 11624–1629, Oct. 2003.

[12] S. J. Hong, J. S. Lee, K. S. Sim, S. M. Kim, D. H. Moon, B. Hong, K. S. Lee, J. W. Park, S. Park, M. C. Lee, J. G. Choe, and J. T. Rhee, "Improving DOI information using 3-layer crystlas for small animal PETs," in *Proc. IEEE NSS-MIC Conf.*, 2004, vol. 4, pp. 2434–2438.

[13] J. S. Lee, S. J. Hong, S. M. Kim, K. S. Sim, B. Hong, K. S. Lee, D. H. Moon, S. Park, J. G. Ghoe, J. T. Rhee, D. S. Lee, J.-K. Chung, and M. C. Lee, "Design, simulation, and reconstruction strategies for small animal PET scanner with 3-layer phoswich crystals and PMT with large effective are ratio," *J. Nucl. Med.*, vol. 46, p. 491P, 2005.

[14] S. Shimizu, K. Kurashige, T. Usui, N. Shimura, K. Sumiya, N. Senguttuvan, A. Gunji, M. Kamada, and H. Ishibashi, "Scintillation properties of $Lu_{0.4}$ $Gd_{1.6}$ $SiO_5$ :Ce (LGSO) crystal," in *Proc. IEEE NSS-MIC Conf.*, 2004, vol. 5, pp. 2734–2736.

[15] K. Kitamura, T. Yamaya, E. Yoshida, T. Tsuda, N. Inadama, and H. Murayama, "Preliminary design studies of a high sensitivity small animal DOI-PET scanner: jPET-RD," in *Proc. IEEE NSS-MIC Conf.*, 2004, vol. 6, pp. 3896–3900.

[16] T. Tsuda, H. Murayama, K. Kitamura, N. Inadama, T. Yamaya, E. Yoshida, F. Nishikido, M. Hamamoto, H. Kawai, and Y. Ono, "Performance evaluation of a subset of a four-layer LSO detector for a small animal DOI PET scanner: jPET-RD," *IEEE Trans. Nucl. Sci.*, vol. 53, no. 1, pp. 35–39, Feb. 2006.

[17] R. S. Miyaoka, S. G. Kohlmyer, and T. K. Lewellen, "Performance characteristics of micro crystal element (MiCE) detectors," *IEEE Trans. Nucl. Sci.*, vol. 48, no. 4, pp. 1403–1407, Aug. 2001.

[18] S. Siegel, W. S. Robert, Y. Shao, and S. R. Cherry, "Simple charge division readouts for imaging scintillator arrays using a multi-channel PMT," *IEEE Trans. Nucl. Sci.*, vol. 43, no. 3, pp. 1634–1641, Jun. 1996.

[19] C. M. Pepin, P. Berard, A. L. Perrot, C. Pepin, D. Houde, R. Lecomte, C. L. Melcher, and H. Dautet, "Properties of LYSO and recent LSO scintillators for phoswich PET detectors," *IEEE Trans. Nucl. Sci.*, vol. 51, no. 3, pp. 789–795, Jun. 2004.